



## Two-Phase Transients of Polymer Electrolyte Fuel Cells

Yun Wang<sup>\*,a</sup> and Chao-Yang Wang<sup>\*,z</sup>

Electrochemical Engine Center and Department of Mechanical and Nuclear Engineering,  
The Pennsylvania State University, University Park, Pennsylvania 16802, USA

A three-dimensional transient model fully coupling the two-phase flow, species transport, heat transfer, and electrochemical processes was developed to study the dynamics of gas-diffusion layer (GDL) dewetting and its impact on polymer electrolyte fuel cell performance. It was found that the dewetting of fuel cells by dry gas is characterized by several regimes of different time constants. These regimes can be classified by through-plane drying vs in-plane drying as well as by the differing water diffusivity in the anode and cathode. The water diffusivity in the anode GDL is several times larger than that in the cathode, therefore the anode side undergoes faster water loss to the dry gas stream. In addition, the land hampers the diffusive transport of water, therefore the liquid water tends to be trapped under the land and the water loss there starts only after through-plane drying of the GDL under the channel is completed. The different time constants of various dewetting regimes also affect the evolution of cell voltage due to the ohmic loss in the membrane. In addition, theoretical solutions are developed for the in-plane and through-plane drying regimes, and show good agreement with the numerically predicted time scales.

© 2007 The Electrochemical Society. [DOI: 10.1149/1.2734076] All rights reserved.

Manuscript submitted September 14, 2006; revised manuscript received February 21, 2007. Available electronically May 7, 2007.

One of the most complex and vital phenomena in polymer electrolyte fuel cells (PEFCs) is the transients of two-phase transport.<sup>1</sup> Liquid water may block pore paths of mass transport through porous gas diffusion layers (GDL) and catalyst layers, thereby reducing PEFC performance and leading to cell degradation.<sup>2,3</sup> In addition, water is needed for the proton conductivity of the membrane to lower the Ohmic loss. Thus, proper water management is crucial for optimization of cell performance. Transients of water accumulation in the membrane, catalyst layers, and GDLs are of paramount importance to water management and dynamic responses of PEFC engines.

While transients of both GDL flooding and dewetting are of great interest in understanding PEFC dynamics, this study considers the transient phenomenon of dewetting of a flooded GDL in a PEFC by feeding with dry gas. That is, when a PEFC with flooded GDLs switches from highly humidified gases to drier gases, what happens to the water distribution in the GDL and how does the cell voltage respond? Another practical problem of the same fundamental nature is the use of dry streams to remove the residual water in the fuel cell after PEFC shutdown for avoidance of possible degradation due to water freezing in the cold environment. This is referred to as gas purge after PEFC engine shutdown. GDL dewetting under such conditions is controlled by the two-phase transient phenomena with phase change. Furthermore, because heat transfer always interacts with phase change two-phase flow, the nonisothermal conditions must be considered in the exploration of GDL dewetting.

Mathematical modeling of heat transfer and two-phase transport in a PEFC has been carried out by several groups. Yuan and Sundén<sup>4</sup> presented a nonisothermal, two-phase model in multidimensional (multi-D) situations. However, only the cathode GDL and gas channel were considered. Costamagna<sup>5</sup> also developed a multi-D model in which phase change heat transfer was ignored. Berning and Djlali<sup>6</sup> presented a two-phase model considering heat release/absorption due to phase change and using the unsaturated flow theory (UFT)<sup>7</sup> which assumes a constant gas-phase pressure. Mazumder and Cole<sup>8</sup> developed a model for hydrophilic GDLs without explicit description of water transport through the membrane in their model. Birgersson et al.<sup>9</sup> recently presented a nonisothermal separate flow model, consisting of separate equations to describe water transport in liquid and gas phases. However, they ignored entropic heat and irreversible heat generation from electrochemical reactions, and also treated the catalyst layer as an interface, thus failing to accurately address the coupling between two-phase and thermal

transport processes in PEFCs. Most recently, Wang and Wang<sup>10</sup> developed a three-dimensional (3D) nonisothermal two-phase model for PEFCs and introduced new physical concepts of heat and water transport in the catalyst layer and GDL, i.e., vapor-phase diffusion of water and heat pipe effect, for the first time. Their work indicates that these two mechanisms primarily take place in the in-plane direction and the vapor-phase diffusion can transport a comparable amount to the water production rate.

The above reviewed literature mostly focuses on steady state operation. Studies of transient transport and electrochemical processes in a PEFC have been attempted by fewer groups. Um et al.,<sup>11</sup> Yan et al.,<sup>12</sup> and Shimpalee et al.<sup>13</sup> explored a type of transients due to gas reactant transport to the catalytic sites, which typically occurs in the sub-second range. A comprehensive study on dynamics of electrochemical double layer discharging/charging, gas transport, and membrane hydration/dehydration was carried out by Wang and Wang.<sup>14</sup> The membrane hydration/dehydration was found to dominate the PEFC transients under low humidity. Their subsequent work<sup>15</sup> further incorporated the electron transport equation into the transient 3D model to study the dynamics under load/current change. Severe undershoot of cell voltage was found during the current rise. All of the above transient models consider single-phase transport only. A two-phase, one-dimensional (1D) transient model was attempted by Ziegler et al.,<sup>16</sup> who developed a two-phase model to study the effect of liquid water formation and transport on the current-voltage characteristics of PEFCs under isothermal conditions. Another 1D transient nonisothermal two-phase model developed by Song et al.<sup>17</sup> only considers the water and oxygen transport in the cathode GDL, while ignoring water balance between the anode and cathode. Also, the validity of a two-phase, nonisothermal analysis along the through-plane direction is highly questionable, as is shown shortly.

The objective of the present work was to develop a 3D transient nonisothermal two-phase model to study the problem of GDL dewetting and explore the intricate interactions between the two-phase flow and thermal transport as well as their impact on cell dynamics. A detailed membrane electrode assembly (MEA) model is used to describe the co-transport of water and protons in the membrane and electrodes. Two-dimensional (2D) numerical simulations, along with a theoretical analysis, were performed.

### Two-Phase Transient Model

A PEFC model consists of five principles of conservation: mass, momentum, energy, species, and charge. These can be presented in concise form as follows

$$\text{Continuity equation: } \nabla \cdot (\rho \vec{u}) = 0 \quad [1]$$

\* Electrochemical Society Active Member.

<sup>a</sup> Present address: Department of Mechanical and Aerospace Engineering, University of California at Irvine, Irvine, CA 92697-3975, USA.

<sup>z</sup> E-mail: cwx31@psu.edu

**Table I. Source terms for the conservation equations in each region.**

	$S_u$	$S_k$	$S_{\Phi_e}$	$S_{\Phi_s}$
Gas channels	0	0	–	0
Diffusion layers	$-\frac{\mu}{K_{\text{GDL}}}\vec{u}$	0	0	0
Catalyst layer	$-\frac{\mu}{K_{\text{CL}}}\vec{u}$	$-\nabla \cdot \left( \frac{n_d}{F} \vec{t}_e \right) - \frac{s_k j}{n_k F}$	$j$	$-j$
Membrane	–	0	0	–
Electrochemical reaction: $\sum s_k M_k^z = n e^-$ In PEFCs, there are: (anode) $\text{H}_2 - 2\text{H}^+ = 2e^-$ (cathode) $2\text{H}_2\text{O} - \text{O}_2 - 4\text{H}^+ = 4e^-$		where	$\begin{cases} M_k \equiv \text{chemical formula of species } k \\ s_k \equiv \text{stoichiometry coefficient} \\ n \equiv \text{number of electrons transferred} \end{cases}$	

Note:  $n_d$  is the electro-osmotic drag coefficient for water. For  $\text{H}_2$  and  $\text{O}_2$ ,  $n_d = 0$ .

Momentum conservation:

$$\frac{\rho}{\varepsilon} \left[ \frac{\partial \vec{u}}{\partial t} + \frac{1}{\varepsilon} \nabla \cdot (\vec{u}\vec{u}) \right] = -\nabla_p + \nabla \cdot \tau + S_u \quad [2]$$

Energy conservation:

$$\frac{\partial \bar{\rho} c_p T}{\partial t} + \nabla \cdot (\gamma_T \rho c_p \vec{u} T) = \nabla \cdot (k^{\text{eff}} \nabla T) + S_T \quad [3]$$

Species conservation ( $\text{H}_2\text{O}/\text{H}_2/\text{O}_2$ ):

$$\begin{aligned} & \varepsilon^{\text{eff}} \frac{\partial C^k}{\partial t} + \nabla \cdot (\gamma_c \vec{u} C^k) \\ &= \nabla \cdot (D_g^{\text{eff}} \nabla C_g^k) - \nabla \cdot \left[ \left( \frac{m f_1^k}{M^k} - \frac{C_g^k}{\rho_g} \right) \vec{j}_1 \right] + S_k \end{aligned} \quad [4]$$

$$\text{Charge conservation (electrons): } 0 = \nabla \cdot (\sigma^{\text{eff}} \nabla \Phi_s) + S_{\Phi_s} \quad [5]$$

$$\text{Charge conservation (protons): } 0 = \nabla \cdot (\kappa^{\text{eff}} \nabla \Phi_e) + S_{\Phi_e} \quad [6]$$

where  $\rho$ ,  $\vec{u}$ ,  $p$ ,  $T$ ,  $C^k$ ,  $\Phi_s$ , and  $\Phi_e$ , respectively, denote the density, superficial fluid velocity vector, pressure, temperature, molar concentration of species  $k$ , electronic phase potential, and electrolyte phase potential. The current transient model is the expansion upon the steady-state two-phase  $M^2$  model formulated by Wang and Wang,<sup>10</sup> therefore details of the modeling assumptions and description at steady state are given in Ref. 10. Experimental validation of the steady state two-phase model was carried out by Wang et al.<sup>18</sup> for both carbon paper and carbon cloth GDLs. In addition, a negligible mass source/sink in the continuity equation is assumed as justified in Ref. 19. A complete form of the electron/proton transport

equation should include a transient term representing electrochemical double layer charging. However, as discussed in Ref. 14 and 15, the time constant of the double layer discharging/charging ranges from micro- to milliseconds, sufficiently short to be safely neglected for automotive fuel cells. Another assumption made in the present model is the water vapor interfacial equilibrium during transient condensation/evaporation. This can be justified by calculating the time scale of local chemical equilibrium which can be estimated from  $r_p/aD^w$  according to Wang et al.,<sup>20</sup> where  $r_p$  is the pore radius,  $a$  the liquid-vapor interfacial area which is in turn proportional to  $1/r_p$ , and  $D^w$  the water vapor diffusivity in gas. For the GDL pore radius of 10  $\mu\text{m}$  and water vapor diffusivity of the order of  $10^{-5} \text{ m}^2/\text{s}$ , the time scale to reach local interfacial equilibrium is 10  $\mu\text{s}$ , sufficiently short to justify the assumption in the present transient model dealing with physical events longer than 10 ms.

The electrochemical properties and the source terms,  $S_u$ ,  $S_k$ ,  $S_{\Phi_e}$ , and  $S_{\Phi_s}$ , are summarized in Tables I and II in detail. Additional parameters are given in Table III.

*Nonisothermal two-phase transport.*—Detailed discussion of two-phase transport at steady states can be found in Ref. 10 and is therefore not repeated here. Other properties related to two-phase transients, the focus of the present work, are elaborated below. The two-phase mixture density is defined as

$$\rho = s\rho_l + (1-s)\rho_g \quad [7]$$

where the liquid water saturation,  $s$ , is the volume fraction of open pores occupied by liquid water. In the  $M^2$  model, the liquid saturation is obtained from the following relation with the mixture water concentration,  $C^{\text{H}_2\text{O}}$ , after the latter is solved from the governing equation (Eq. 4)

$$s = \frac{C^{\text{H}_2\text{O}} - C_{\text{sat}}}{\rho_l/M^{\text{H}_2\text{O}} - C_{\text{sat}}} \quad [8]$$

**Table II. Electrochemical properties.**

Description	Anode	Cathode
Transfer current density, $j$ ( $\text{A}/\text{m}^2$ )	$a_{i_0,a} \left( \frac{C_{\text{H}_2}}{C_{\text{H}_2,\text{ref}}} \right)^{1/2} \left( \frac{\alpha_a + \alpha_c}{RT} \cdot F \cdot \eta \right)$	$-a_{i_0,c} \left( \frac{C_{\text{O}_2}}{C_{\text{O}_2,\text{ref}}} \right) \exp \left( -\frac{\alpha_c F}{RT} \cdot \eta \right)$
Surface overpotential, $\eta$ (V)	$\Phi_s - \Phi_e - U_o$	$\Phi_s - \Phi_e - U_o$
Equilibrium potential, $U_o$ (V)	0	$1.23 - 0.9 \times 10^{-3} (T - 298)$
Exchange current density $\times$ reaction surface area, $a_0 i_0$ ( $\text{A}/\text{m}^2$ )	$1.0 \times 10^9$	$10^4$
Transfer coefficient, $\alpha$	$\alpha_a + \alpha_c = 2$	$\alpha_c = 1$

Table III. Geometrical, physical, and operating parameters.

Quantity	Value
Gas channel depth/width	0.5/1.0 mm
Shoulder width	1.0 mm
GDL thickness, $\delta_{\text{GDL}}$	0.2 mm
Catalyst layer thickness, $\delta_{\text{CL}}$	0.01 mm
Membrane thickness, $\delta_{\text{m}}$	0.018 mm
Anode/cathode pressures, $P$	2.0/2.0 atm
Stoichiometry, $\xi_{\text{a}}/\xi_{\text{c}}$ @ 1.0 A/cm <sup>2</sup>	150.0/200.0
Inlet temperature of gas flows, $T_0$	353.15 K
Porosity of GDLs/catalyst layers, $\varepsilon$	0.6/0.4
Volume fraction of ionomer in catalyst layers, $\varepsilon_{\text{m}}$	0.26
Activation energy for oxygen reduction reaction, $E_{\text{a}}$	73269 J/mol
Thermal conductivity of membrane, $k_{\text{mem}}^{\text{eff}}$	0.95 W/m K
Thermal conductivity of catalyst layer/GDL, $k_{\text{CL}}^{\text{eff}}/k_{\text{GDL}}^{\text{eff}}$	3.0/3.0 W/m K
Thermal conductivity of bipolar plate, $k_{\text{land}}^{\text{eff}}$	20.0 W/m K
Specific heat of catalyst layers/GDLs, $c_p^{\text{CL}}/c_p^{\text{GDL}}$	709/709 J/kg K
Specific heat of water, $c_p^{\text{l}}$	4182 J/kg K
Specific heat of membrane, $c_p^{\text{mem}}$	500 J/kg K
Viscosity of liquid water, $\mu_{\text{l}}$	$3.5 \times 10^{-4}$ kg/m s
Surface tension, liquid-water-air (80°C), $\sigma$	0.0625 N/m
Contact angle, $\theta_{\text{c}}$	110°
Permeability of GDL, $K_{\text{GDL}}$	$10^{-12}$ m <sup>2</sup>
Liquid-vapor phase change latent heat, $h_{\text{fg}}$	$2.26 \times 10^6$ J/kg

Heat generation in the energy equation, Eq. 3, due to the electrochemical processes and phase change, can be summarized as

$$\text{In the catalyst layer: } S_T = j \left( \eta + T \frac{dU_o}{dT} \right) + \frac{i_{\text{e}}^2}{\kappa^{\text{eff}}} + \frac{i_{\text{s}}^2}{\sigma^{\text{eff}}} + S_{\text{fg}}$$

$$\text{In the membrane: } S_T = \frac{i_{\text{e}}^2}{\kappa^{\text{eff}}}$$

$$\text{In the GDL: } S_T = \frac{i_{\text{s}}^2}{\sigma^{\text{eff}}} + S_{\text{fg}}$$

$$\text{In the bipolar plate: } S_T = \frac{i_{\text{s}}^2}{\sigma^{\text{eff}}} \quad [9]$$

The heat release/absorption due to water condensation/evaporation,  $S_{\text{fg}}$ , is given by

$$S_{\text{fg}} = h_{\text{fg}} \dot{m}_{\text{fg}} \quad [10]$$

where  $h_{\text{fg}}$  is the latent heat of liquid-vapor phase change and  $\dot{m}_{\text{fg}}$  is the phase change rate. The latter is readily calculated from the liquid continuity equation, namely

$$\dot{m}_{\text{fg}} = \rho_{\text{l}} \frac{\partial s}{\partial t} + \nabla \cdot (\rho_{\text{l}} \vec{u}_{\text{l}}) \quad [11]$$

where the liquid-phase velocity in the M<sup>2</sup> model is computed from

$$\rho_{\text{l}} \vec{u}_{\text{l}} = \vec{j}_1 + \lambda_{\text{l}} \rho \vec{u} \quad [12]$$

where  $\vec{j}_1$  is the capillary diffusion flux calculated by

$$\vec{j}_1 = \frac{\lambda_{\text{l}} \lambda_{\text{g}}}{v} K [\nabla P_{\text{c}} + (\rho_{\text{l}} - \rho_{\text{g}}) \vec{g}] \quad [13]$$

The Leverett function is generally used to express the relationship between capillary pressure and liquid saturation in porous media, namely

$$P_{\text{c}} = P_1 - P_{\text{g}} = \sigma \cos(\theta_{\text{c}}) \left( \frac{\varepsilon}{K} \right)^{1/2} J(s) \quad [14]$$

where,  $\sigma$  is the surface tension and  $J(s)$  is given by

$$J(s) = \begin{cases} 1.417(1-s) - 2.120(1-s)^2 + 1.263(1-s)^3 & \text{for } \theta_{\text{c}} < 90^\circ \\ 1.417s - 2.120s^2 + 1.263s^3 & \text{for } \theta_{\text{c}} > 90^\circ \end{cases} \quad [15]$$

Note that Leverett  $J$ -function only considers the influence of two characteristics of a porous medium, i.e., porosity and permeability, while ignoring the effect of detailed pore morphology.<sup>21</sup>

In addition, the relative mobilities of individual phases,  $\lambda_{\text{k}}$ , are

$$\lambda_{\text{l}} = \frac{k_{\text{rl}}/v_{\text{l}}}{k_{\text{rl}}/v_{\text{l}} + k_{\text{rg}}/v_{\text{g}}} \quad \text{and} \quad \lambda_{\text{g}} = 1 - \lambda_{\text{l}} \quad [16]$$

where the relative permeabilities,  $k_{\text{rl}}$  and  $k_{\text{rg}}$ , are defined as the ratio of the intrinsic permeability of liquid and gas phases, respectively, to the total intrinsic permeability of a porous medium. Physically, these parameters describe the extent to which one fluid is hindered by others in pore spaces, and hence can be formulated as a function of liquid saturation. Most of previous work adopted cubic relations. Here, we take the following formula for the relative permeabilities, which are most recently employed by Luo et al.<sup>22</sup>

$$k_{\text{rl}} = s^4 \quad \text{and} \quad k_{\text{rg}} = (1-s)^4 \quad [17]$$

Finally, in the energy equation, Eq. 3,  $\bar{\rho}c_p$  is the average over the ones of solid matrix, liquid water and gas phase, given by

$$\bar{\rho}c_p = (1-\varepsilon)\rho^s c_p^s + \varepsilon s \rho^{\text{l}} c_p^{\text{l}} + \varepsilon(1-s)\rho^{\text{g}} c_p^{\text{g}} \quad [18]$$

In addition, the specific capacity of two phase mixture,  $c_p$ , in the convection term of Eq. 3 is defined as

$$c_p = \frac{s \rho^{\text{l}} c_p^{\text{l}} + (1-s)\rho^{\text{g}} c_p^{\text{g}}}{\rho} \quad [19]$$

In the presence of liquid water in the catalyst layer, the electrochemically active area is modified as follows

$$a i_0 = (1-s) a_0 i_{0,T} \quad [20]$$

In addition, temperature affects the reaction rate of the oxygen reduction reaction (ORR) and the exchange current density,  $a_0 i_{0,T,c}$  can be expressed in Arrhenius form as follows

$$a_0 i_{0,T,c} = a_0 i_{0,c} \exp \left[ - \frac{E_{\text{a}}}{R} \left( \frac{1}{T} - \frac{1}{353.15} \right) \right] \quad [21]$$

where  $E_{\text{a}}$  denotes the activation energy for ORR at the Pt/Nafion electrode as provided by Parthasarathy et al.<sup>23</sup>

*Water accumulation in the membrane.*— Water molecules in the membrane exist in a state of attaching to the hydrophilic sulfuric acid groups. The time constant,  $\tau_{\text{m}}$ , for membrane hydration is  $\sim 20$  s for Nafion 112 or  $\sim 8$  s for Gore 18  $\mu\text{m}$  membrane, which is longer than those of gas transport ( $\tau_{\text{D}} \sim 0.01$ – $0.1$  s) and electrochemical double layer discharging/charging ( $\tau_{\text{db}} \sim 1$   $\mu\text{s}$ – $1$  ms).<sup>14,15</sup>

In addition, there exists ionomer or electrolyte phase in the catalyst layer. Therefore, water accumulation also takes place in the electrodes. The effect of water accumulation in the MEA is described through the effective factor,  $\varepsilon^{\text{eff}}$ , in Eq. 4

$$\varepsilon^{\text{eff}} = \varepsilon_{\text{g}} + \varepsilon_{\text{m}} \frac{dC_{\text{w}}^{\text{m}}}{dC_{\text{w}}} = \varepsilon_{\text{g}} + \varepsilon_{\text{m}} \frac{\rho_{\text{m}} RT}{EW p^{\text{sat}} da} \quad [22]$$

where  $\rho_{\text{m}}$  is the density of a dry membrane. Note that Eq. 4 encompasses the water transport equation in the MEA as well as GDL and gas channels.

*Boundary/initial conditions.*— Equations 1-6 form a complete set of governing equations with ten unknowns:  $\vec{u}$  (three components),  $p$ ,  $T$ ,  $C^{\text{H}_2}$ ,  $C^{\text{O}_2}$ ,  $C^{\text{H}_2\text{O}}$ ,  $\phi_{\text{e}}$ , and  $\phi_{\text{s}}$ . Their corresponding boundary conditions can be found in Ref. 10 and are therefore not repeated here. The initial conditions are either uniformly zero or follow the steady-state distributions corresponding to the operating point at the start of a transient process.

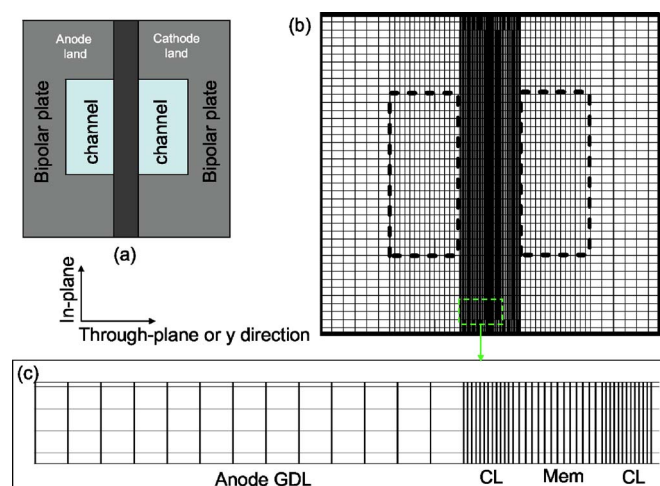


**Figure 1.** (Color online) Computational domain and mesh of a differential PEFC.

**Numerical procedures.**— The governing equations, Eq. 1-6, along with their appropriate boundary conditions are discretized by the finite volume method<sup>24</sup> and solved in a commercial flow solver, Fluent (version 6.0.12), by PISO algorithm (the pressure implicit splitting of operators).<sup>25</sup> PISO is based on predictor-corrector splitting for unsteady problems. The source terms and physical properties are programmed into user-defined functions (UDF), based on the software user-coding capability. In addition, overall species balance is checked in addition to the equation residuals as important convergence criteria. These species balance checks also ensure physically meaningful results. In the simulations to be presented below, values of species imbalance (i.e., H<sub>2</sub>, O<sub>2</sub>, and H<sub>2</sub>O) are all less than 1% and equation residuals smaller than 10<sup>-6</sup>. Adaptive time stepping is used in which the current time step is inversely proportional to the temporal gradient of cell voltage at the previous time step, with the maximum of 0.1 s.

### Numerical Results

Due to the computational intensiveness of transient simulations, a 2D PEFC or a cross-section of a single-channel PEFC, usually referred as to a differential fuel cell, is selected to study the PEFC dewetting, as shown in Fig. 1. The 2D geometry is a minimal requirement for studies of nonisothermal, two-phase phenomena including the vapor-phase diffusion and heat pipe effect.<sup>10</sup> In the two-phase zone, the flux of vapor-phase diffusion can be expressed, in the vector form, as

$$D_g^{w,eff}(T,P) \nabla C^w = D_g^{w,eff}(T,P) \nabla C_{sat}(T) = D_g^{w,eff}(T,P) \frac{dC_{sat}}{dT} \nabla T \quad [23]$$

It can be seen that the vapor-phase diffusion flux is directly proportional to the thermal gradient. Figure 2 shows the temperature gradient vector in the cross-section of the cathode GDL. Clearly, the vapor-phase diffusion, important for water management in a fuel cell, takes place mostly in the in-plane direction. Thus, a 2D geometry, i.e., in-plane plus through-plane directions, is required to capture this vital mechanism for water transport under nonisothermal situations. The heat pipe effect, induced by the vapor-phase diffusion, also occurs mostly in the in-plane direction, as given by

$$h_{fg} \dot{m}_{fg} = h_{fg} M_w D_g^{w,eff}(T,P) \frac{dC_{sat}(T)}{dT} \nabla T = k_{fg}(T,P) \nabla T \quad [24]$$

The initial condition for the following transient simulation is the steady state under a full humidification operation. Of interest is the transient process after switching to dry operation, i.e., *RH a/c*

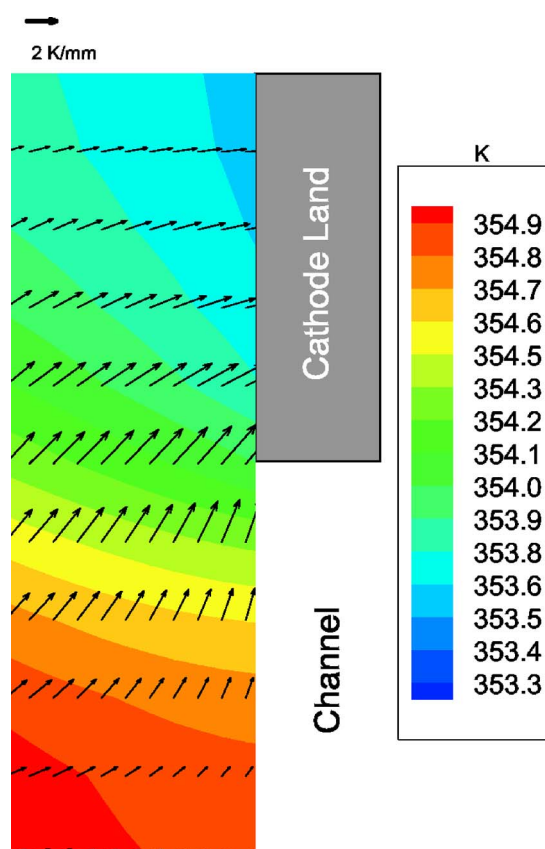


**Figure 2.** (Color online) Thermal gradient vectors in the cathode GDL.

= 50/50%, under a constant average current density, 1.0 A/cm<sup>2</sup>. The gas flow rates (or stoichiometric ratios) in the anode and cathode are large for a differential fuel cell, thus channel flooding is absent.

Figure 3 displays the time responses of cell voltage and membrane resistance upon the change in the inlet gas humidity. It can be seen that the cell voltage experiences four major stages of decrease as marked in the figure. The cell voltage drop can be explained by the membrane resistance evolution plotted in the same figure. Note

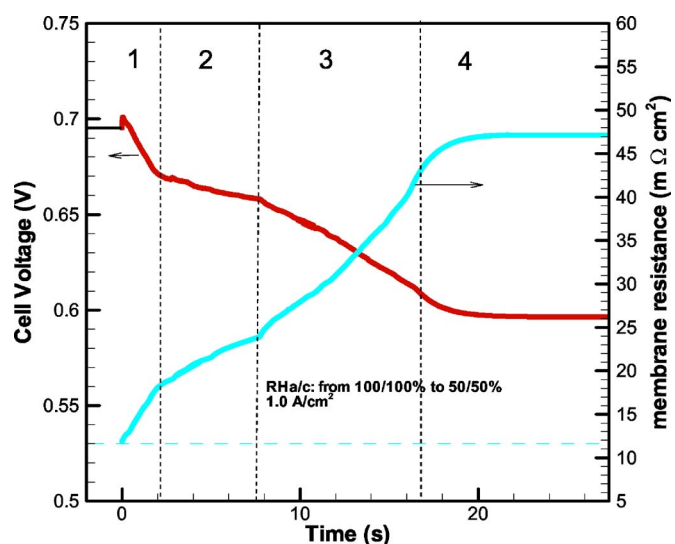


**Figure 3.** (Color online) Time evolutions of cell voltage and membrane resistance.

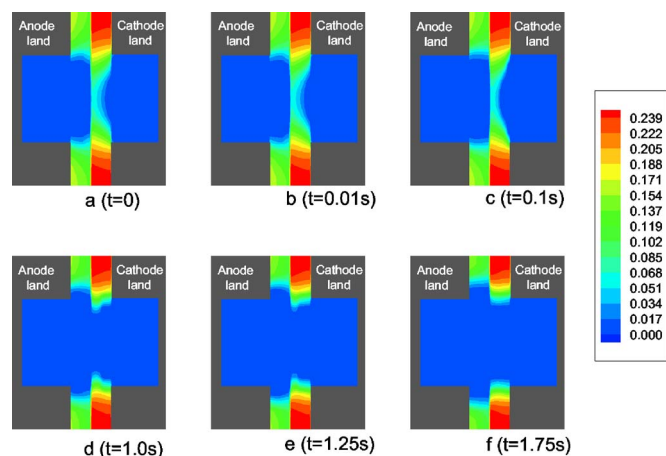
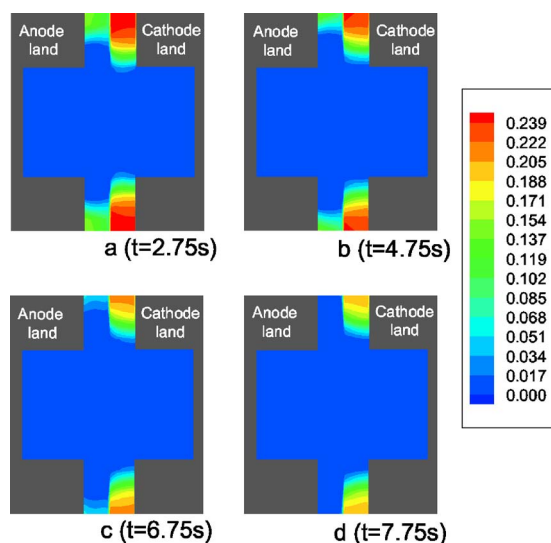


**Figure 4.** (Color online) Liquid water saturation distributions at time instants of 0, 0.01, 0.1, 1.0, 1.25, and 1.75 s.

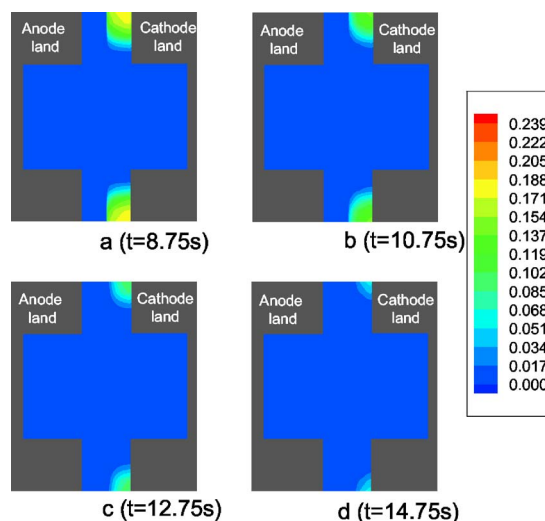
that the cell performance in this range of the current is controlled by the Ohmic loss. The membrane resistance increase is due to the switch to drier gas, which gradually dries up liquid water inside the fuel cell.

Figure 4 shows the distributions of liquid water saturation at different time instants in stage 1. Figure 4a is at the initial condition, the steady state of full humidification operation. Under the initial condition, liquid water exists in both anode and cathode. Upon the change to the 50% RH gas in both anode and cathode channels, liquid water in the GDL under the channel is first evaporated and removed by the dry gas. This first stage of dewetting can be characterized as through-plane drying under the channel, i.e., the evaporation front moving inward in the through-plane direction. In addition, it can be seen that the liquid water level under the land changes little even though the level under the channel experiences a significant decrease.

The GDL dewetting under the channel is followed by in-plane drying under the land. Because the water diffusivity in the anode is several times larger than in the cathode, in-plane drying in the anode GDL takes place faster. The evolution of liquid water saturation in stage 2 of anode in-plane drying is displayed in Fig. 5. This figure shows that liquid water is evaporated away from the anode GDL



**Figure 5.** (Color online) Liquid water saturation distributions at time instants of 2.75, 4.75, 6.75, and 7.75 s.



**Figure 6.** (Color online) Liquid water saturation distributions at time instants of 8.75, 10.75, 12.75, and 14.75 s.

under the land and the evaporation front propagates from the channel area into the land area. The process in stage 2 takes  $\sim 5$  s.

Obviously, water loss under the land occurs simultaneously in both cathode and anode sides. However, the cathode in-plane drying takes longer due to the lower water diffusivity in the cathode. Note that the duration of cathode in-plane drying encompasses both stages 2 and 3. In addition, in stage 2, liquid water remains under the lands of both sides, thus the resulting increase in the average membrane resistance and loss in cell voltage are relatively small. Once liquid water disappears in the anode under both channel and land after stage 2, the rise in membrane resistance accelerates as shown in Fig. 3 during stage 3. Figure 6 displays the evolution of the water saturation contours in stage 3, indicative of in-plane drying in the cathode. At this stage, liquid water in the cathode GDL underneath the land is removed via two mechanisms: one is evaporation at the evaporation front and the other is water back-diffusion through the membrane to the dry anode.

Figure 7 displays the water concentration in the gas phase at two time instants in stage 3. It can be seen that even though the liquid water region in the cathode shrinks significantly, the water concentration in the gas phase remains high in the GDL. Consequently, the membrane still maintains a certain level of hydration. Once all liquid water disappears and there is no water supply from evaporation, membrane dehydration accelerates, resulting in the final stage of cell voltage or membrane resistance evolution during the dewetting process, as shown in Fig. 3. The membrane dehydration can take several seconds. Figure 8 displays the water concentration distributions in the GDL at three time instants in stage 4. It is seen that water concentrations throughout the fuel cell are below the saturation

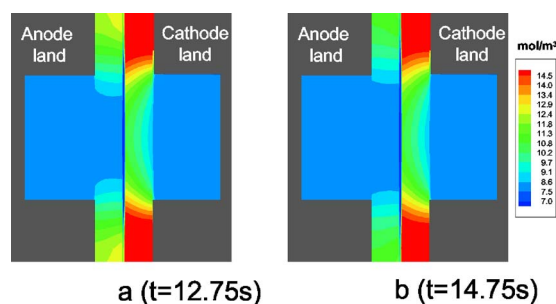


**Figure 7.** (Color online) Water vapor concentration contours at time instants of 12.75 and 14.75 s.

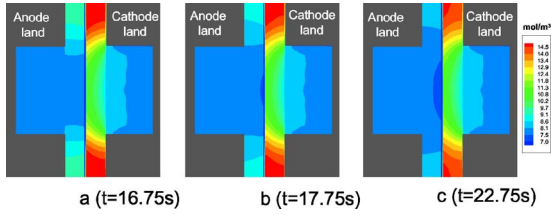


**Figure 8.** (Color online) Water vapor concentration contours at time instants of 16.75, 17.75, and 22.75 s.

value at 80°C, i.e., 15.9 mol/m<sup>3</sup>. In addition, the GDL maintains a relatively higher value of water concentration on both anode and cathode at 16.75 s and the water concentration falls quickly over the subsequent seconds until reaching the steady state at 22.75 s.

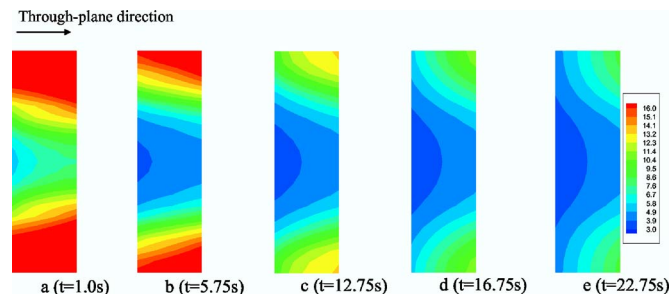
Figure 9 shows the water content distributions in the membrane at each of four stages. It can be seen that the dewetting process of GDLs and catalyst layers is followed by membrane dehydration. The latter is the main reason for the increase of the membrane resistance and cell voltage drop as shown in Fig. 3. In addition, the underland region always maintains a higher water content than the underchannel region. At 5.75 s in stage 2 when the GDL dewetting under the channel is completed, there is a large difference between the underland and the underchannel water content. From 16.75 to 22.75 s when there is no liquid water in the fuel cell, i.e., in stage 4, the membrane content decreases, indicative of dehydration.

Figure 10 displays the evolution of current density contours. It can be seen that initially high current density appears under the channel. This is due to the full-humidity operation at  $t = 0$ , which maintains a high water content in the membrane, rendering the Ohmic resistance relatively small. Therefore the oxygen transport limitation dominates the local cell performance. As the GDL dewets under the channel, the local membrane resistance increases, leading to a shift of the current density peak from the underchannel to the underland area. The difference between the current densities under the land and channel is further increased until 5.75 s, in consistency with the occurrence of maximum non-uniformity in membrane water content, as shown in Fig. 9. After 5.75 s, GDL in-plane drying towards the land area increases the local membrane resistance and hence the difference in the local current density between the channel and land areas diminishes.

#### GDL Drying: Analysis

As displayed by the foregoing numerical results, the differential fuel cell structure, i.e., 2D land-to-channel configuration, undergoes two regimes of dewetting through-plane drying followed by in-plane drying. Here we develop analytical solutions for both drying regimes in order to shed further light on the fundamental characteristics of through-plane and in-plane drying.

*Through-plane drying.*— Figure 11a sketches the through-plane drying process. For the GDL two-phase region with an average liq-



**Figure 9.** (Color online) Water content contours in the membrane at time instants of 1.0, 5.75, 12.75, 16.75, and 22.75 s.

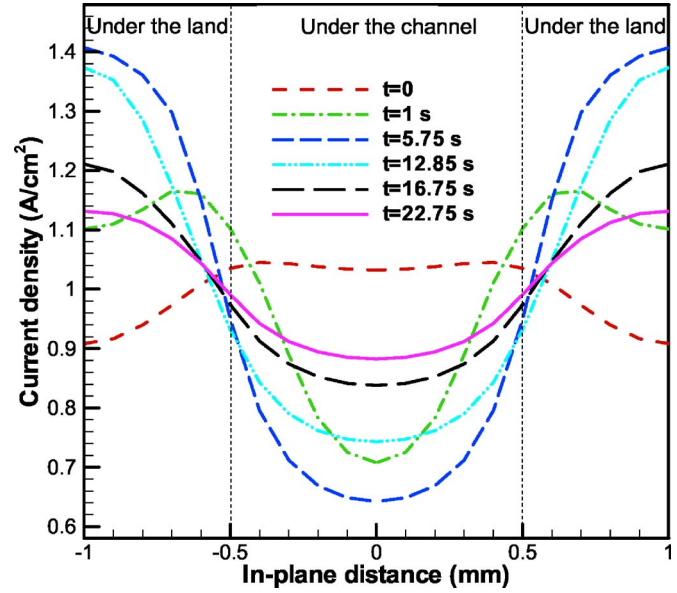


**Figure 10.** (Color online) Evolution of current density profiles.

uid saturation  $s_0$ , assuming there exist water supply from the catalyst layer and water vapor removal from the evaporation front, the law of water balance gives rise to

$$(1 + 2\alpha) \frac{I}{2F} - D_g^{w,eff} \frac{\Delta C}{\delta} = \frac{d}{dt} \left[ (\delta_{GDL} - \delta) \frac{\varepsilon s_0 \rho_l}{M^{H_2O}} \right] \quad [25]$$

where,  $s_0$  is the average liquid water saturation in the two-phase zone prior to drying. Define  $Y = \delta/\delta_{GDL}$  and rearrange the above equation as

$$(1 + 2\alpha) \frac{I}{2F} - D_g^{w,eff} \frac{\Delta C}{\delta_{GDL}} \frac{1}{Y} = \frac{\varepsilon s_0 \rho_l \delta_{GDL}}{M^{H_2O}} \left( -\frac{dY}{dt} \right) \quad [26]$$

Define

$$\tau = \frac{t}{t_1} \quad \text{where } t_1 = \frac{\varepsilon s_0 \rho_l (\delta_{GDL})^2}{2D_g^{w,eff} M^{H_2O} \Delta C} \quad \text{and } R = \frac{(1 + 2\alpha) I \delta_{GDL}}{2F D_g^{w,eff} \Delta C} \quad [27]$$

one has

$$R - \frac{1}{Y} = -2 \frac{dY}{d\tau} \quad [28]$$

The dimensionless parameter,  $R$ , measures the ratio of the water addition rate due to ORR to the water removal rate from the two-phase region. Therefore, when  $R < 1$ , the dewetting process can dry up a flooded GDL completely, while when  $R > 1$ , only part of the GDL can be dewetted. The solution to Eq. 28 at  $RY < 1$  can be derived as

$$\tau = -\frac{2}{R} Y - \frac{2}{R^2} \ln(1 - RY) \quad [29]$$

When  $R \rightarrow 0$

$$\ln(1 - RY) = -RY - \frac{(RY)^2}{2} + O(R^3) \quad [30]$$

Therefore

$$\tau = Y^2 + O(R) \quad \text{when } R \rightarrow 0 \quad [31]$$

When  $R = 0$ , e.g., at open circuit, one arrives at

$$\tau = Y^2 \quad \text{or } Y = \sqrt{\tau} \quad [32]$$

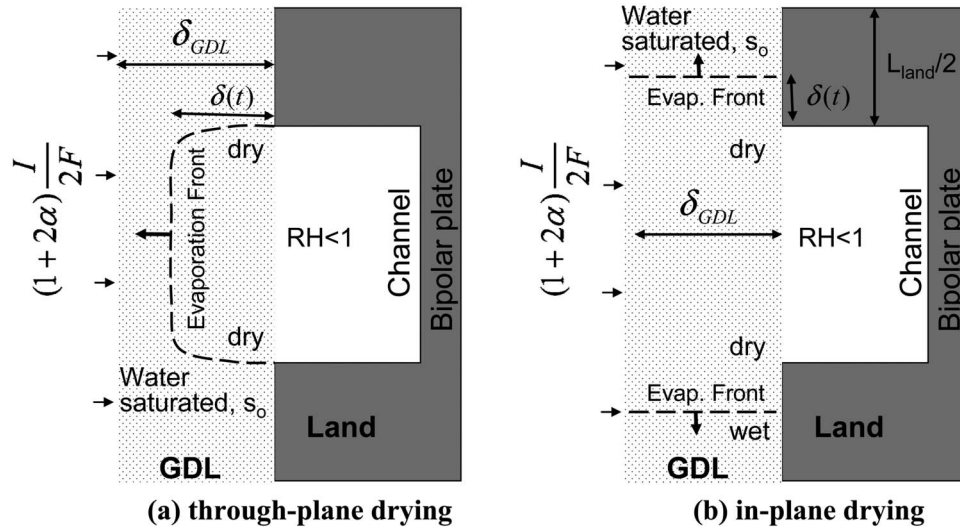


Figure 11. Schematics of GDL (a) through-plane and (b) in-plane drying.

When  $Y = 1$ , i.e., the through-plane dewetting is completed,  $\tau = 1$ .

In addition, assuming the gaseous water concentration at the evaporation front is equal to the saturation value and channel flow is at infinite rate, it follows that

$$\Delta C = C_{\text{sat}}(1 - RH) \quad [33]$$

Therefore

$$t_1 = \frac{s_o \rho_1 (\delta_{\text{GDL}})^2}{2D_g^w \varepsilon^{n-1} M^{\text{H}_2\text{O}} C_{\text{sat}}(1 - RH)} \quad [34]$$

$$R = \frac{(1 + 2\alpha)I\delta_{\text{GDL}}}{2FD_g^w \varepsilon^{n-1} C_{\text{sat}}(1 - RH)}$$

where  $n$  is the Bruggeman factor accounting for tortuosity of the diffusion paths in the GDL, and  $RH$  the relative humidity of the channel gas. In addition,  $t_1$  can be regarded as the time constant for the through-plane drying upon the fuel cell shutdown or  $R = 0$ , which depends on the GDL thickness, porosity, gas  $RH$  in the channel, and  $C_{\text{sat}}(T)$  or local temperature.

Graphs of  $Y$  vs  $\tau$  are plotted in Fig. 12 for different values of  $R$ . It can be seen that the  $Y$ - $\tau$  curve is highly dependent on  $R$ , especially as  $R$  approaches unity. Under the condition of the numerical simulation case,  $R = \sim 0.2$ , therefore the time for through-plane drying, i.e.,  $Y = 1$  or  $\tau = \sim 1.2$ , is  $\sim 1.5$  s, which is of the same magnitude as the duration of stage 1 shown in Fig. 3.

*In-plane drying.*—Figure 11b schematically shows the in-plane drying process on the cathode side. Following the same approach as for through-plane drying, one can obtain

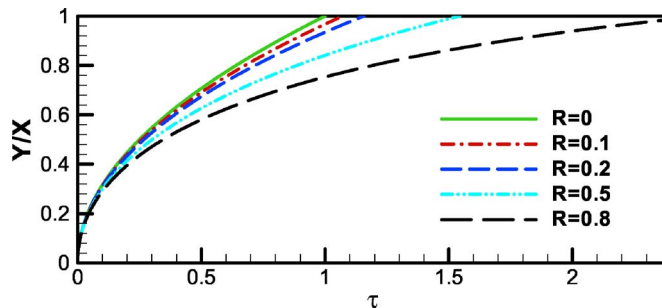


Figure 12. (Color online) Graphs of  $Y$  or  $X$  vs  $\tau$ .

$$(1 + 2\alpha) \frac{I}{2F} \frac{L_{\text{land}}}{2} - D_g^{\text{w,eff}} \frac{\Delta C}{\delta} \delta_{\text{GDL}} = \frac{d}{dt} \left[ \left( \frac{L_{\text{land}}}{2} - \delta \right) \delta_{\text{GDL}} \frac{\varepsilon s_o \rho_1}{M^{\text{H}_2\text{O}}} \right] \quad [35]$$

Define  $X = \delta/L_{\text{land}/2}$  and rearrange the above equation as

$$(1 + 2\alpha) \frac{I}{2F} \frac{L_{\text{land}}}{2} - \frac{D_g^{\text{w,eff}} \Delta C \delta_{\text{GDL}}}{\frac{L_{\text{land}}}{2}} \frac{1}{X} = - \frac{L_{\text{land}}}{2} \frac{\delta_{\text{GDL}} \varepsilon s_o \rho_1}{M^{\text{H}_2\text{O}}} \frac{dX}{dt} \quad [36]$$

Define

$$\tau = \frac{t}{t_2} \quad \text{where } t_2 = \frac{\varepsilon s_o \rho_1 \left( \frac{L_{\text{land}}}{2} \right)^2}{2D_g^{\text{w,eff}} M^{\text{H}_2\text{O}} \Delta C}$$

$$= \frac{s_o \rho_1 \left( \frac{L_{\text{land}}}{2} \right)^2}{2D_g^w \varepsilon^{n-1} M^{\text{H}_2\text{O}} C_{\text{sat}}(1 - RH)} \quad \text{and } R = \frac{(1 + 2\alpha)I L_{\text{land}}}{2F \frac{2}{D_g^{\text{w,eff}} \Delta C} \delta_{\text{GDL}}}$$

$$= \frac{(1 + 2\alpha)I \left( \frac{L_{\text{land}}}{2} \right)^2}{2F D_g^{\text{w,eff}} \Delta C \delta_{\text{GDL}}} \quad [37]$$

one has

$$R - \frac{1}{X} = -2 \frac{dX}{d\tau} \quad [38]$$

Comparing Eq. 38 and 28, it is clear that the dynamics of in-plane and through-plane drying share the same mathematical characteristics. Thus, Eq. 29 and Fig. 12 also describe the in-plane drying process, provided that the location of the evaporation front is normalized by their respective length scales. In addition, one can obtain the following relationship between  $t_1$  and  $t_2$

$$t_2 = t_1 \left( \frac{L_{\text{land}}/2}{\delta_{\text{GDL}}} \right)^2 \quad [39]$$

In the simulation case or according to Table I,  $t_2 = 6.25t_1$  for the same value of  $s_o$ . In addition,  $t_2$  is inversely proportional to  $D_g^w$  as shown in Eq. 37. Thus, the time constant of in-plane drying in the anode is roughly three times shorter than that in the cathode based on the different water diffusivities given in Ref. 10.

## Conclusions

A transient model fully coupling two-phase flow, transport, heat transfer, and electrochemical phenomena has been developed to investigate the dynamics of GDL dewetting and its impact on PEFC performance. A 2D numerical study was carried out to unravel the dynamics of liquid water transport in GDLs, catalyst layers, and membrane, upon a step change in the gas humidification conditions, from  $RH\ a/c = 100/100\%$  to  $50/50\%$ , designed to dewet flooded GDLs. The simulation results indicate that the dewetting of fuel cells by dry gas undergoes various stages of different time constants, due to the differing water diffusivity in the anode from the cathode as well as to through-plane drying vs in-plane drying. The water diffusivity in the anode GDL was several times larger than that in the cathode; therefore the anode side undergoes faster water loss to the dry gas flow. In addition, the land hampers the diffusive transport of reactant/water; therefore the liquid water is trapped under the land and the water loss there starts only after through-plane drying of the GDL under the channel is completed. The differing time constants of various dewetting regimes also impact the evolution of cell voltage due to the ohmic loss. In addition, the analytical solutions were developed to describe in-plane and through-plane drying and were found to be in good agreement with the numerical prediction of the time constants.

## Acknowledgments

Partial support of this work by Ford Motor Company, Penn State Materials Research Institute, and NSF grant no. 0609727 is gratefully acknowledged.

The Pennsylvania State University assisted in meeting the publication costs of this article.

## List of Symbols

$A$	electrode area, $m^2$
$a$	water activity; effective catalyst area per unit volume, $m^2/m^3$
$a_o$	catalyst surface area per unit volume, $m^2/m^3$
$C_k$	molar concentration of species $k$ , $mol/m^3$
$c_p$	specific heat, $J/kg\ K$
$D$	species diffusivity, $m^2/s$
EW	equivalent weight of dry membrane, $kg/mol$
$F$	Faraday's constant, $96,487\ C/equivalent$
$I$	current density, $A/cm^2$
$i$	superficial current density, $A/cm^2$
$j$	transfer current density, $A/cm^2$
$\vec{j}_l$	mass flux of liquid phase, $kg/m^2\ s$
$K$	permeability, $m^2$
$k$	thermal conductivity, $W/m\ K$
$k_r$	relative permeability
$L$	length, $m$
$M$	molecular weight, $kg/mol$
$m_j^k$	mass fraction of species $k$ in liquid phase
$n$	the direction normal to the surface
$n_d$	electro-osmotic coefficient, $H_2O/H^+$
$P$	pressure, $Pa$
$R$	universal gas constant, $8.134\ J/mol\ K$
$S$	source term
$s$	stoichiometry coefficient in electrochemical reaction or liquid saturation
$t$	time, $s$
$T$	temperature, $K$
$U_o$	equilibrium potential, $V$
$\vec{u}$	velocity vector, $m/s$
$V_{cell}$	cell potential, $V$

## Greek

$\alpha$	transfer coefficient; net water flux per proton flux
$\rho$	density, $kg/m^3$
$\nu$	kinematic viscosity, $m^2/s$
$\theta_c$	contact angle, $^\circ$
$\phi$	phase potential, $V$
$\kappa$	proton conductivity, $S/m$
$\xi$	stoichiometric flow ratio
$\lambda$	membrane water content
$\lambda_k$	mobility of phase $k$
$\epsilon$	porosity
$\eta$	surface overpotential, $V$
$\tau$	shear stress, $N/m^2$
$\gamma_c$	correction factor for species convection
$\gamma_T$	correction factor for thermal convection
$\delta$	thickness, $m$
$\sigma$	electronic conductivity, $S/m$ ; or surface tension, $N/m$

## Superscripts and Subscripts

$a$	anode
$c$	cathode; capillary
CL	catalyst layer
$D$	diffusion
db	double layer
$e$	electrolyte
eff	effective value
fg	phase change
$g$	gas phase
GDL	gas diffusion layer
in	inlet
$k$	species; liquid or gas phase
$l$	liquid
$m$	membrane phase
$o$	gas channel inlet value; reference value
ref	reference value
$s$	solid
sat	saturate value
$w$	water

## References

1. C. Y. Wang, *Chem. Rev. (Washington, D.C.)*, **104**, 4727 (2004).
2. D. P. Wilkison and J. St-Pierre, in *Handbook of Fuel Cells: Fundamentals, Technology and Applications*, W. Vielstich, H. Gasteiger, A. Lamm, Editors, John Wiley & Sons, New York, (2003).
3. X. G. Yang, F. Y. Zhang, A. Lubawy, and C. Y. Wang, *Electrochem. Solid-State Lett.*, **7**, 408 (2004).
4. J. Yuan and B. Sunden, *Electrochim. Acta*, **50**, 677 (2004).
5. P. Costamagna, *Chem. Eng. Sci.*, **56**, 323 (2001).
6. T. Berning and N. Djilali, *J. Electrochem. Soc.*, **150**, A1589 (2003).
7. C. Y. Wang and P. Cheng, *Adv. Heat Transfer*, **30**, 93 (1997).
8. S. Mazumder and J. V. Cole, *J. Electrochem. Soc.*, **150**, 1510 (2003).
9. E. Birgersson, M. Nojonen, and M. Vynnycky, *J. Electrochem. Soc.*, **152**, A1021 (2005).
10. Y. Wang and C. Y. Wang, *J. Electrochem. Soc.*, **153**, A1193 (2006).
11. S. Um, C. Y. Wang, and K. S. Chen, *J. Electrochem. Soc.*, **147**, 4485 (2000).
12. W. Yan, C.-Y. Soong, F. Chen, and H.-S. Chu, *J. Power Sources*, **143**, 48 (2005).
13. S. Shimpalee, W.-k. Lee, J. W. Van Zee, and H. Naseri-Neshat, *J. Power Sources*, **156**, 355 (2006).
14. Y. Wang and C. Y. Wang, *Electrochim. Acta*, **50**, 1307 (2005).
15. Y. Wang and C. Y. Wang, *Electrochim. Acta*, **51**, 3924 (2006).
16. C. Ziegler, H. M. Yu, and J. O. Schumacher, *J. Electrochem. Soc.*, **152**, A1555 (2005).
17. D. Song, Q. Wang, Z.-S. Liu, and C. Huang, *J. Power Sources*, **159**, 928 (2006).
18. Y. Wang, C. Y. Wang, and K. S. Chen, *Electrochim. Acta*, **52**, 3965 (2007).
19. Y. Wang and C. Y. Wang, *J. Electrochem. Soc.*, **152**, 445 (2005).
20. C. Y. Wang, W. B. Gu, and B. Y. Liaw, *J. Electrochem. Soc.*, **145**, 3407 (1998).
21. F. A. L. Dullien, *Porous Media: Fluid Transport and Pore Structure*, Academic Press, San Diego (1992).
22. G. Luo, H. Ju, and C. Y. Wang, *J. Electrochem. Soc.*, **154**, B316 (2007).
23. A. Parthasarathy, S. Srinivasan, and A. J. Appleby, *J. Electrochem. Soc.*, **139**, 2530 (1992).
24. S. V. Patankar, *Numerical Heat Transfer and Fluid Flow*, Hemisphere Publishing, New York (1980).
25. R. I. Issa, *J. Comput. Phys.*, **62**, 40 (1986).